Magnetic dimers and trimers in the disordered $S = \frac{3}{2}$ spin system BaTi$_{1/2}$Mn$_{1/2}$O$_3$

F. A. Garcia,[1,*] U. F. Kaneko,[2] E. Granado,[2] J. Sichelschmidt,[3] M. Hölzel,[4] J. G. S. Duque,[5] C. A. J. Nunes,[6]
R. P. Amaral,[6] P. Marques-Ferreira,[6] and R. Lora-Serrano[6]

[1]*IFUSP, Univ. de São Paulo, 05508-090, São Paulo-SP, Brazil*
[2]*Inst Fis Gleb Wataghin, Univ. Estadual de Campinas, 13083-970, Campinas-SP, Brazil*
[3]*Max Planck Institute for Chemical Physics of Solids, D-01187 Dresden, Germany*
[4]*Forschungsneutronenquelle Heinz Maier-Leibnitz (FRM II), Technische Universität München,*
Lichtenbergstr. 1, D-85747 Garching, Germany
[5]*Nucleo de Física, Campus Itabaiana, UFS, 49500-000, Itabaiana, SE, Brazil*
[6]*Univ. Fed. de Uberlândia, Instituto de Física, 38400-902, Uberlândia-MG, Brazil*
(Received 27 May 2014; revised manuscript received 7 May 2015; published 11 June 2015)

We report a structural-magnetic investigation by x-ray absorption spectroscopy (XAS), neutron diffraction, dc susceptibility (χ_{dc}), and electron spin resonance (ESR) of the 12R-type perovskite BaTi$_{1/2}$Mn$_{1/2}$O$_3$. Our structural analysis by neutron diffraction supports the existence of structural trimers with chemically disordered occupancy of Mn^{4+} and Ti^{4+} ions, with the valence of the Mn ions confirmed by the XAS measurements. The magnetic properties are explored by combining dc-susceptibility and X-band (9.4 GHz) electron spin resonance, both in the temperature interval of $2 \leqslant T \leqslant 1000$ K. A scenario is presented under which the magnetism is explained by considering magnetic dimers and trimers, with exchange constants $J_a/k_B = 200\,(2)$ K and $J_b/k_B = 130\,(10)$ K, and orphan spins. Thus, BaTi$_{1/2}$Mn$_{1/2}$O$_3$ is proposed as a rare case of an intrinsically disordered $S = \frac{3}{2}$ spin gap system with a frustrated ground state.

I. INTRODUCTION

Oxides with perovskite structure are among the most explored systems in condensed matter physics. These materials are suitable for fundamental studies in the field, as well as for technological applications, mostly due to the great number of observed ground states and properties such as multiferroicity, high-temperature superconductivity, colossal magnetoresistance, and many others [1].

The ideal formula unit for a perovskite compound is ABO$_3$, where A is a rare-earth or alkaline-earth cation and B is a smaller transition metal cation (like Ti, Mn, Co, or Ni). When a second (B') metal atom is added to the above structure, an ordered double-perovskite-type structure A_2BB'O$_6$ (where B, $B' = 3d$, $4d$ and/or $5d$ metals) as well as the disordered $AB_{1/2}B'_{1/2}$O$_3$ perovskite structure might be formed. The magnetic properties of both spin and orbital degrees of freedom in these materials are a subject of intense investigation.

In the case of the B-site ordered double perovskites, both the B and B' sites are arranged in interpenetrating face-centered-cubic sublattices. If the B sites are occupied by nonmagnetic ions and the B' sites by magnetic ions constrained to interact antiferromagnetically, the magnetic interactions between the ions at the B' sites will be geometrically frustrated [2]. In this direction, these systems are good platforms for a systematic investigation of frustrated magnetic interactions, which can give rise to the realization of exotic ground states such as the spin glasses, spin liquids, and spin ice phases [3,4]. In the past few years, such investigation was carried out for some of these systems [2,5–7].

In the case of the disordered structures, geometric frustration is not certain. In this context, the partially dis-

ordered 12R-type perovskite BaTi$_{1/2}$Mn$_{1/2}$O$_3$ [8] is noteworthy, mainly due to its low symmetry and high degree of chemical disorder (site occupancy) at the B and B' sites. Indeed, a large Curie–Weiss (θ_{CW}) constant, with no sign of a magnetic phase transition down to $T = 2$ K, was reported for this material [8]. Thus, in BaTi$_{1/2}$Mn$_{1/2}$O$_3$ long-range magnetic order, if it occurs, takes place at a temperature $T \ll \theta_{\mathrm{CW}}$, the hallmark of a frustrated system.

On the other hand, this behavior is not exclusive of geometrically frustrated systems. In some compounds, due to strong short-range interactions, the spins are coupled and form magnetically correlated states, presenting an excitation gap between the $S = 0$ singlet ground state and the $S = 1$ excited state. These are called spin-gap systems, and the field has attracted attention since the pioneering work of Nikuni *et al.* on the Bose–Einstein condensation of magnons in the spin-gap system TlCuCl$_3$ [9].

There is a number of $S = \frac{1}{2}$ or $S = 1$ spin-gap systems with a three-dimensional (3D) structure (for instance, Ba$_3$Cr$_2$O$_8$ and Ba$_3$Mn$_2$O$_8$ [10,11]) that have been proposed and investigated in the past years. However, in BaTi$_{1/2}$Mn$_{1/2}$O$_3$, the Mn cations are all in a 4+ valence state resulting in a set of $S = \frac{3}{2}$ spins. Few examples of spin gap systems have been exhibited in the case of $S = \frac{3}{2}$, among which RCrGeO$_5$ ($R = $ Y or ^{154}Sm) have been recently confirmed as such by an investigation using inelastic neutron scattering [12]. Furthermore, in BaTi$_{1/2}$Mn$_{1/2}$O$_3$ the occupation of one of the transition-metal sites is suggested to be disordered [8], making the system also attractive due to the possibility of investigating the role of disorder in the physics of spin-gap systems [13,14]. In addition, the structure allows the formation of magnetic trimers which, for an antiferromagnetic exchange, will present a frustrated ground state, connecting the physics of spin-gap and frustrated systems.

---

*fgarcia@if.usp.br

In this work, we report x-rays absorption spectroscopy (XAS), neutron diffraction, dc susceptibility, and electron spin resonance of the partially disordered 12R-type perovskite $BaTi_{1/2}Mn_{1/2}O_3$. Our structural analysis supports a scenario where the magnetism of the system depends on the occupation of the transition metal sites at the structural trimers. We propose that at some of these structural trimers, Mn^{4+} spin dimers, and trimers are formed, while a population of "orphan" spins is left behind. Our results strongly suggest that $BaTi_{1/2}Mn_{1/2}O_3$ is a rare case of a $S = \frac{3}{2}$ spin-gap system, with a frustrated ground state. In addition, this is an intrinsically disordered compound.

II. EXPERIMENTAL

Polycrystalline samples of $BaTi_{1/2}Mn_{1/2}O_3$ were synthesized by solid-state reaction. Stoichiometric amounts of $BaCO_3$, MnO_2, and TiO_2 were mixed and grounded in an agate mortar and heated in air at $900\,°C$ for 24 hours in a tubular furnace. The material was then regrounded and heated in air at $1100\,°C$ for 24 hours. After each grounding and heating step, the sample was checked by x-ray diffraction to observe the amount of possible spurious phases. High-purity phases could then be obtained by repetition of the grounding and heat treatment.

The XAS measurements were carried out at the XAFS-1 beamline of the Brazilian Synchrotron Light Laboratory (LNLS), using Si(111) crystals to monochromatize the incident beam. A Mn foil spectrum was recorded simultaneously (in the back channel) so that the edge position of the Mn could be calibrated. The inflection point in the first resolved peak of the Mn foil was chosen to be the absorption edge of the metallic Mn (6539 eV). In this way, the edge shifts of the Mn K edges for all systems in this work could be compared (i.e., the change in valence of the Mn). The data were normalized using ATHENA [15]. For a qualitative comparison, reference samples of the Mn oxides MnO (Mn^{2+}), Mn_2O_3 (Mn^{3+}), and $BaMnO_3$ (Mn^{4+}) were used.

A detailed structural investigation was carried out using the high-resolution powder diffractometer called the Structure Powder Diffractometer (SPODI) at the Heinz Maier–Leibnitz (FRM II) research reactor, employing a Ge(511) monochromator with $\lambda = 1.54832\,(2)$ Å. A closed-cycle cryostat with a base temperature of $T = 3.6$ K was employed for the low-T measurements. The structural refinement of the neutron powder diffraction data for $BaTi_{1/2}Mn_{1/2}O_3$ was performed by means of the Rietveld method with the GSAS+EXPGUI package [16,17].

The magnetic properties of $BaTi_{1/2}Mn_{1/2}O_3$ were investigated by dc-susceptibility (χ_{dc}) and X-band (9.4 GHz) ESR measurements. In the temperature interval $2\,K \leqslant T \leqslant 350\,K$, χ_{dc} was measured by using a Quantum Design superconducting quantum interference device (SQUID) magnetometer. In the high-temperature region, $300\,K \leqslant T \leqslant 1000\,K$, χ_{dc} was measured in a Quantum Design SQUID vibrating sample magnetometer (VSM). Care was taken to use similar sample masses in these measurements and to calibrate the position of the sample in a way that the moment per mol would render the same result at $T = 300$ K using both equipments. The ESR measurements were performed in a commercial Bruker
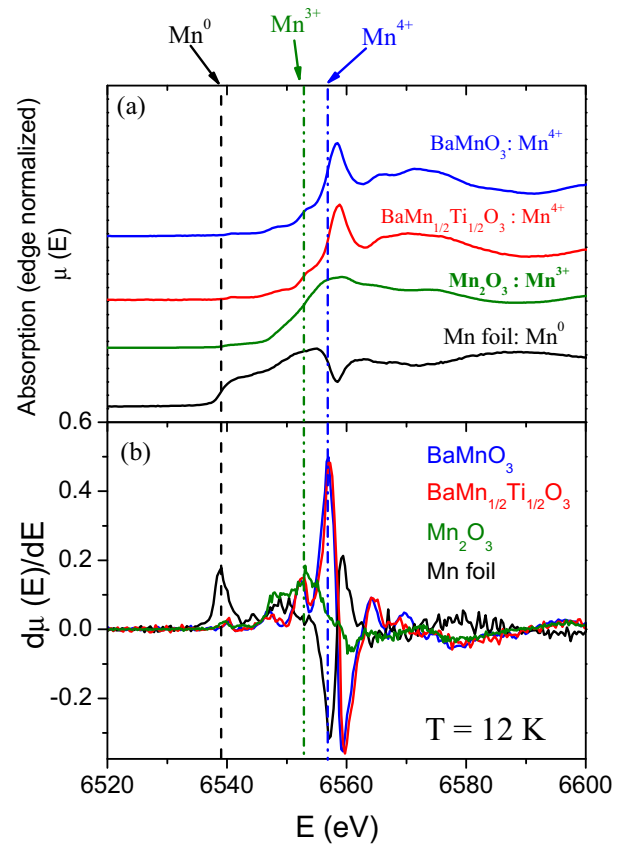

FIG. 1. (Color online) (a) X-ray absorption coefficient and (b) first derivatives of the XAS data (Mn K edge) measured at $T = 12$ K for our $BaTi_{1/2}Mn_{1/2}O_3$ sample (nominal valence of 4+) and the reference samples (standards) Mn foil, Mn_2O_3 (Mn^{3+}) and $BaMnO_3$ (Mn^{4+}).

Elexsys-500 spectrometer. For the interval $2\,K \leqslant T \leqslant 300\,K$, the temperature was controlled by using a conventional He flow cryostat, whereas for the interval $300\,K \leqslant T \leqslant 900\,K$, a N_2 flow system was employed.

III. RESULTS AND DISCUSSION

A. X-ray absorption spectroscopy and neutron diffraction

The results of our XAS investigation are presented in Figs. 1(a) and 1(b). The shapes of the Mn K edges, as well as the edge shifts (>2 eV), are clearly distinguishable in Fig. 1(a), indicating distinct coordination numbers and Mn electronic configurations. Following the discussion in Refs. [18–20], the chemical shift observed in the XAS spectra from $BaTi_{1/2}Mn_{1/2}O_3$ and from $BaMnO_3$ can be compared, suggesting Mn^{4+} cations in our $BaTi_{1/2}Mn_{1/2}O_3$ sample. Figure 1(b) shows the first energy derivative of the absorption coefficient of the XAS spectra from the Mn oxides, which reveals the position of the inflection point of the XAS data in Fig. 1(a). This gives further support for a nearly pure 4+ valence of the Mn cations in $BaTi_{1/2}Mn_{1/2}O_3$ which, in turn, indicates a negligible level of oxygen vacancies in this sample.

Figure 2 shows the observed neutron powder diffraction pattern of $BaTi_{1/2}Mn_{1/2}O_3$ at room temperature (crosses). A
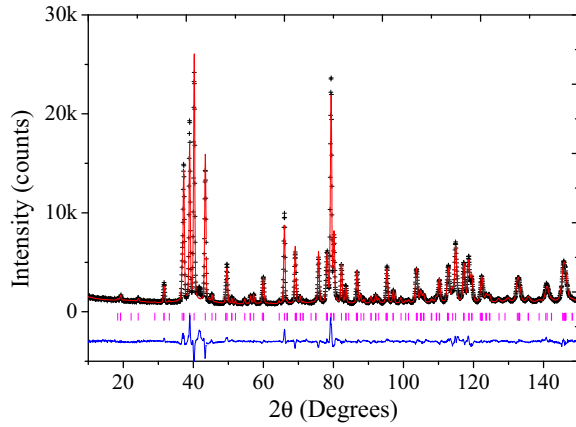
FIG. 2. (Color online) High-resolution neutron powder diffraction pattern of $BaTi_{1/2}Mn_{1/2}O_3$. The cross symbols and solid lines represent observed and calculated patterns, respectively. The difference curve is shown at the bottom. Vertical bars indicate the expected Bragg peak positions according to the nuclear structure model.

FIG. 3. (Color online) Structural model of $BaTi_{1/2}Mn_{1/2}O_3$ with a 12R-type perovskite structure, in which trimers of face-sharing octahedra lying along the c axis are connected by corner-sharing octahedra. The face-sharing octahedron contains two transition metal sites $M(1)$ and $M(2)$. The $M(1)$ are occupied only by Mn atoms (spheres and octahedra in purple), while at the $M(2)$ sites, there is a mixed occupation of Mn and Ti atoms. The $M(3)$ sites are at the center of the corner-sharing octahedra and are occupied exclusively by Ti atoms (spheres and octahedra in blue). The O(1) sites label oxygen sites at the shared face of face-sharing octahedra, whereas O(2) sites are labeling oxygen sites binding face-sharing to corner-sharing octahedra. Two sites for barium are indicated as Ba(1) and Ba(2).

12R-type perovskite structure was employed in the refinement [see Fig. 3(a)]. It consists of face-sharing trimers of octahedra connected by corner-sharing octahedra along the c axis, under the space group $R\bar{3}m$ [8,21]. All atomic occupancy factors were fixed at the stoichiometric values in our Rietveld refinement of the neutron-diffraction data. This procedure is supported by our XAS investigation and avoids instabilities in our fit due to correlations of such factors with thermal parameters.

In this structure, there are three independent transition-metal sites M, all of them surrounded by oxygen octahedra [see Fig. 3(a)]. The $M(1)$ and $M(2)$ sites are located at the center and at the border of the trimers, respectively, while the $M(3)$ site lies outside the trimers and is in the center of the corner-sharing octahedra connecting the trimers. The calculated diffraction pattern (line) under this model is also displayed in Fig. 2, showing good agreement with the experimental data.

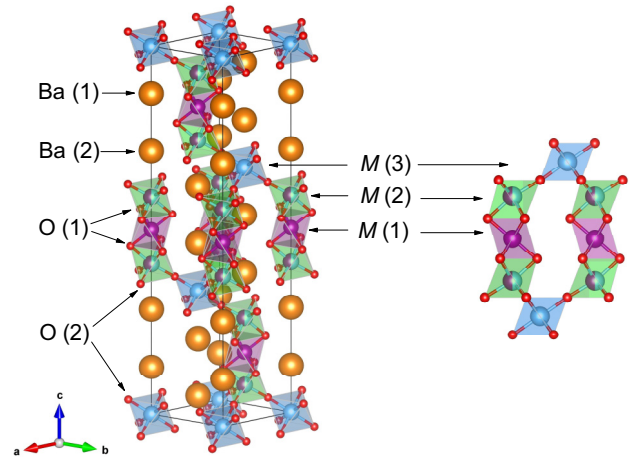The refinement results and relevant bond distances are given in Table I. A good agreement of the atomic positions and bond distances is found with respect to previously published data [8,21].

It should be noted that, due to the close similarity between the coherent scattering lengths for Ti and Mn, the relative occupancy of these atoms in the $M(1)$, $M(2)$, and $M(3)$ transition metal sites (see Fig. 2) cannot be directly determined from our refinements. However, this information can be inferred from the bond distances extracted from the refinement results [8,22]. In fact, in an octahedral coordination, the expected Mn^{4+}-O^{2-} and Ti^{4+}-O^{2-} covalent bond lengths are 1.930 and 2.005 Å [22], respectively. In Table I it is shown that the M(1)-O(1) bond length equals 1.922(2) Å, being close to the Mn^{4+}-O^{2-} bond length, thus suggesting this site is Mn rich.

TABLE I. Refined structural parameters and relevant bond lengths for $BaTi_{1/2}Mn_{1/2}O_3$ at room temperature.

Atom	Site	Occupancy	x	y	z	B_{iso} (Å^2)
Ba(1)	6c	1.0	0	0	0.2856 (2)	0.76 (9)
Ba(2)	6c	1.0	0	0	0.1290 (2)	0.12 (6)
M(1)(Mn)	3b	1.0	0	0	0.5	0.0 (1)
M(2)(Ti/Mn)	6c	0.5/0.5	0	0	0.4091 (2)	0.2 (1)
M(3)(Ti)	3a	1.0	0	0	0	0.1 (1)
O(1)	18f	1.0	0.1513 (2)	0.8487 (2)	0.45656 (8)	0.42 (4)
O(2)	18f	1.0	0.1673 (3)	0.8327 (3)	0.62700 (9)	0.63 (4)
			M(1)-O(1) 1.922 (2) Å			
			M(2)-O(1) 1.995 (5) Å			
			M(2)-O(2) 1.932 (4) Å			
			M(3)-O(2) 1.976 (3) Å			

Note: space group $R\bar{3}m$, $a = 5.6910\ (3)$ Å, $b = 5.6910\ (3)$ Å, $c = 27.915\ (1)$ Å, $R_{wp} = 8.0\%$, $R_p = 6.0\%$, $V = 783.0\ (1)$ Å^3.
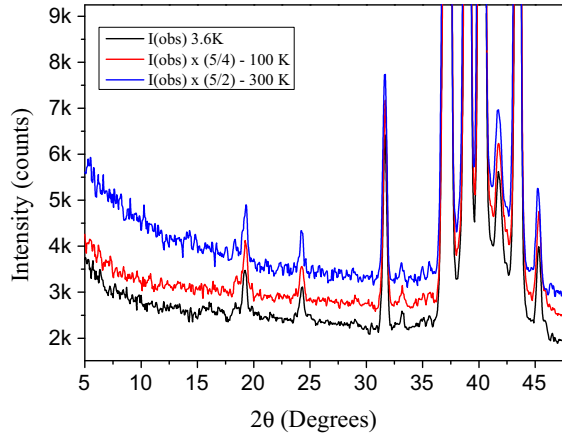
FIG. 4. (Color online) Comparison between the observed high-resolution neutron powder diffraction patterns of BaTi$_{1/2}$Mn$_{1/2}$O$_3$ measured at $T = 3.6$ K (black line), $T = 100$ K (red line), and $T = 300$ K (blue line). Magnifying factors, indicated in the figure, and an offset of the vertical axis were used for better visualization. The profile at $T = 300$ K was obtained by using a sample changer in air and the upturn in the very-low-angle region is due air scattering. No extra features are observed in the diffraction pattern in this low-angle region in the whole T interval investigated.

The M(3)-O(2) bond length reads 1.976(3) Å, being somewhat smaller than the expected Ti^{4+}-O^{2-} bond length.

Therefore, our results do not discard the possibility of a mixed occupancy at the $M(3)$ site. However, it is likely that this site is Ti rich. As for the $M(2)$ site, the $M(2)$-O(1) bond length is 2.005(4) Å, while the $M(2)$-O(2) bond length is 1.925(4) Å, consistent with a mixed occupancy of Mn and Ti atoms at this site. In view of this analysis, the final refinement was performed by assuming a pure occupation at the $M(1)$ (Mn atoms) and $M(3)$ (Ti atoms) sites, and a mixed occupation (Mn and Ti atoms) at the $M(2)$ site (see Table I). This analysis supports the structural model first proposed in Ref. [8].

Figure 4 shows in detail the neutron powder diffraction patterns at low angles for selected temperatures. It can be seen that no additional feature in the profile is found at low T, indicating the absence of long-range magnetic order down to $T = 3.6$ K. This is most likely related to the presence of the Ti^{4+} cations at the $M(3)$ sites, which breaks the 3D exchange isolating the $M(2)$-$M(1)$-$M(2)$ trimers from one another. Hence, all the magnetic properties stem from these isolated, or somewhat weakly coupled, structural trimers and should be determined by the arrangement of the Mn^{4+} and Ti^{4+} cations at these sites.

B. Susceptibility

A measurement of χ_{dc} up to $T = 350$ K was previously reported by Keith *et al.* [8], where an analysis based on the Curie–Weiss law applied to a restricted T interval ($250 \leqslant T \leqslant 350$) K was presented. Such analysis led to an effective moment $\mu_{eff} = 3.92_B$, closely corresponding to the full moments of Mn^{4+} in the sample. In Fig. 5(a), we compare this analysis (dashed line) with our experimental results for $(\chi_{dc} - \chi_0)^{-1}$, where χ_0 is the diamagnetic contribution of the core electrons, in a wide temperature range.
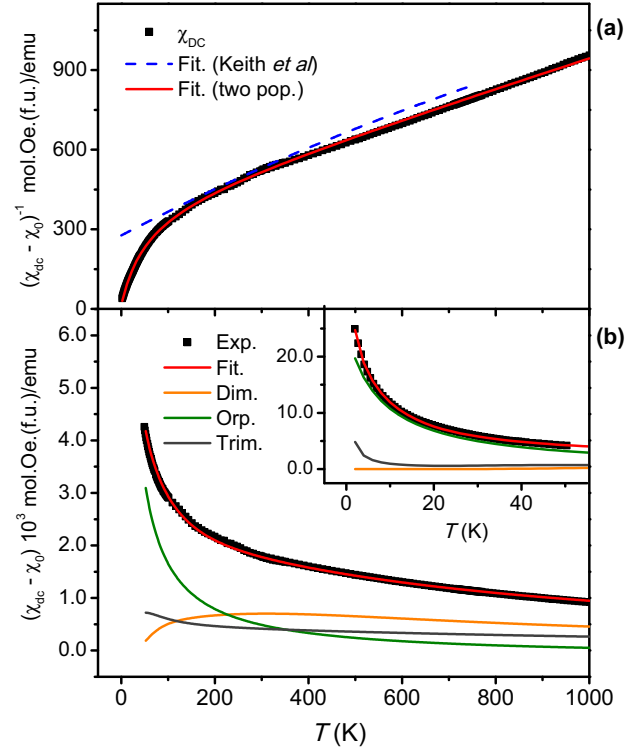

FIG. 5. (Color online) Magnetic properties from dc susceptibility (χ_{dc}) of BaTi$_{1/2}$Mn$_{1/2}$O$_3$. (a) The dashed blue line reproduces the analysis of Ref. [8], which describes the data only in a limited T region; the thick red line is a fitting of the data to a two-population model [23]. (b) $(\chi_{dc} - \chi_0)$ and the fitting of the data to the dimer plus trimer model (thick red line), along with the separated contributions χ_{orp} (thick green line), χ_{dim} and χ_{trim} (thick orange and gray lines, respectively). The inset shows in detail the data and the distinct contributions for $T \leqslant 50$ K. Results for χ_{dim} and χ_{trim} are obtained by considering the quantum Hamiltonians in Eqs. (4) and (5).

On top of the deviation observed at the high-T region, there is a conspicuous drop on $(\chi - \chi_0)^{-1}$ for $T < 200$ K, and the system clearly fails to follow a paramagnetic behavior in the low-T region. This drop on $(\chi - \chi_0)^{-1}$ is reminiscent of the overall behavior of the susceptibility of frustrated systems [3,4]. In the present case, where the magnetism stems from the Mn^{4+} cations occupying the transition metal sites at the trimers, it is possible that part of these cations could take part in some correlated spin state. Hence, one is tempted to adopt a phenomenological two-population model [23] to describe our $(\chi - \chi_0)^{-1}$ data. The data is then fit [solid line in Fig. 5(a)] by using the following phenomenological model:

$$(\chi_{dc} - \chi_0)^{-1} = \left[\left(\frac{C_1}{T + \theta_1} \right) + \left(\frac{C_2}{T + \theta_2} \right) \right]^{-1}, \quad (1)$$

where C_1 (C_2) and θ_1 (θ_2) stands, respectively, for the Curie constant and Curie–Weiss constant to be associated with the correlated (orphan) spins in the system. Since, ideally, the orphan spins are uncorrelated, one expects $\theta_2 = 0$. In practice it is usually found that $\theta_1 \gg \theta_2$ [23]. The following parameters are obtained: $C_1 = 1.68$ emu K/mol (f.u.) Oe, $\theta_1 = 788$ K, $C_2 = 0.12$ emu K/mol (f.u.) Oe and $\theta_2 = 1.86$ K. The

constant contribution χ_0 was not fit. Instead, we estimated $\chi_0 = -0.00029$ emu/mol (f.u.) [24], and this value was used. Please observe that we present the data normalized per formula unit (f.u.) and therefore for one mol of $BaTi_{1/2}Mn_{1/2}O_3$ we have $\frac{1}{2}$ mol of Mn^{4+} cations.

Since the model offers a fair description of the data, it supports the existence of orphan and correlated spin populations, to be associated with distinct energy scales. The nature of the correlated spin state is rooted in the occupancy of the transition metal sites in the structural trimers and depends on how all the possible configurations are combined. The structural trimers may be formed by three Mn atoms, two Mn atoms plus one Ti atom, or one Mn atom plus two Ti atoms. In the first and second configurations, respectively, we propose that magnetic trimers and dimers are formed. The interaction takes place by means of three different exchange paths along the face-sharing octahedra, allowing a strong magnetic coupling between the $M(1)$ and $M(2)$ sites. Under these assumptions, it can be inferred that the orphan spins will amount to $\frac{1}{8}$ of Mn^{4+} cations in the sample, while all other cations will be in some correlated state.

This idea is tested by fitting χ_{dc} over the entire temperature range by using the following model:

$$\chi_{dc} = \chi_0 + \chi_{orp} + \chi_{dim} + \chi_{trim}, \qquad (2)$$

where χ_{orp} is the orphan spin contribution and χ_{dim} and χ_{trim} are, respectively, the contribution from the magnetic dimers and trimers. We adopt a Curie–Weiss susceptibility to model the orphan spin contribution:

$$\chi_{orp} = C/(T + \theta). \qquad (3)$$

The contribution of the magnetic dimers and trimers are deduced by adopting that the interaction among the spins can be described by Heisenberg-type Hamiltonians. For the dimers we write

$$\mathcal{H}_{dim} = J_a S_1 \cdot S_2, \qquad (4)$$

and, for the trimers,

$$\mathcal{H}_{trim} = J_a S_1 \cdot S_2 + J_a S_2 \cdot S_3 + J_b S_1 \cdot S_3. \qquad (5)$$

In Eqs. (4) and (5), J_a and J_b are the first- and second-neighbor exchange constants. In principle one expects $J_b \ll J_a$; however, there is large multiplicity of the exchange paths connecting the transition-metal sites (see Fig. 3) making it possible for J_a and J_b to be comparable. In this regard, it must be noted that for antiferromagnetic J_a and J_b, Eq. (5) describes a magnetic frustrated system. This frustration is important since it reduces the low-temperature magnetic response of the trimer which, otherwise, would diverge much too fast to be related with our experimental results. At a qualitative level, the relation between J_a and J_b can be captured by a classical calculation of the energy of the trimers, which will depend only on the angles between the spins [25]:

$$E = -2J_a \left(\cos \theta_{12} + \cos \theta_{23} + \frac{J_b}{J_a} \cos \theta_{13} \right). \qquad (6)$$

Within this qualitative scenario, the ground state is obtained by a variational calculation to find the angles θ_{ij} which minimizes E as a function of the fraction J_b/J_a. For $0 \leqslant$
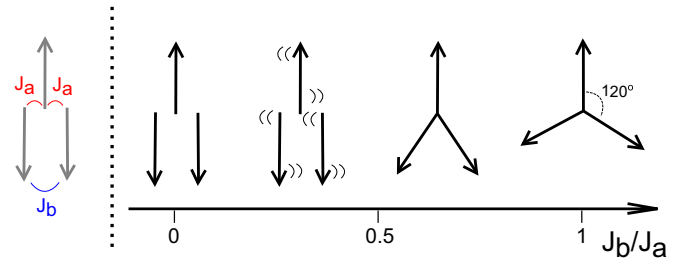

FIG. 6. (Color online) Qualitative scenario for the magnetic properties of the trimers. On the left panel, it is represented that for antiferromagnetic J_a and J_b the trimer is frustrated. On the right panel, a pictorial view of the classical calculation is given. It is only for $J_b/J_a > 0.5$ that the spins will not be in a colinear configuration, making the total spin less than $S = \frac{3}{2}$. The minimum energy and magnetic response occurs for $J_b/J_a = 1$, and the spins would be found in a triangular arrangement for which $S = \frac{1}{2}$.

$J_b/J_a \leqslant 0.5$, one finds that the spins will be aligned in an antiparallel configuration, with J_b being ineffective at lowering the magnetic response of the system. However, for $J_b/J_a > 0.5$, the spins will not be colinear. The lowest possible energy takes place for $J_b = J_a$, with the spins aligned in a triangular arrangement. The discussion is summarized in Fig. 6.

Although the classical calculation offers some insight into the problem, the relation between J_a and J_b in our system must be obtained by considering in full the eigenvalues of the quantum Hamiltonians in Eqs. (4) and (5). The response to the applied field is calculated by perturbation theory, from which the susceptibilities due to the magnetic dimers and trimers are obtained. The total susceptibility [χ_{dc}, defined in Eq. (2)] is compared to the data to obtain the values of J_a and J_b that best describe the experiment.

The resulting fitting, along with the experimental data and the separated contributions from χ_{orp}, χ_{dim}, and χ_{trim}, is shown in Fig. 5(b). The overall picture is very encouraging. The following parameters are obtained from this fitting: $\chi_0 = -0.00014(1)$ emu/mol (f.u.) Oe, $C = 0.19(2)$ emu K/mol (f.u.) Oe, $\theta = 7.7(2)$ K, $J_a/k_B = 200(2)$ K, and $J_b \approx 0.65 J_a$.

The value of χ_0 is less than the one estimated theoretically and may reflect a small, constant, paramagnetic Van Vleck contribution. The orphan spin Curie constant $C = 0.19(4)$ emu K/mol (f.u.) is close to the value of $C = 0.125$ emu K/mol (f.u.) Oe, which can be anticipated for 1/8 of orphan spins. As expected, $\theta = 7.7(2)$ K is a small energy scale, expressing the correlation among the orphan spins. The values for the exchange constants, $J_a/k_B \approx 200$ K and $J_b \approx 0.65 J_a$, are close to values determined for others 3D spin-gap systems [26,27]. The size of J_b is of the correct magnitude to be effective in decreasing the magnetic response of the trimer. The inset in Fig. 5(b) shows in detail the results for $T \leqslant 50$ K.

C. Electron spin resonance

The single-ion physics and qualitative aspects of the effects of electron correlations can be captured by electron spin resonance measurements. The ESR parameters of interest

are the ESR g-values ($g = h\upsilon/\mu_0 H_{\rm res}$), where $H_{\rm res}$ is the resonance field, and the ESR linewidth, ΔH, which is proportional to the peak-to-peak distance of the derivative of the absorption spectrum.

Some representative ESR spectrum lines are shown in Fig. 7(a). A careful inspection of the spectra reveals a partial distortion of some spectrum lines, especially the one for $T = 9$ K. This observation suggests the use of a powder profile fitting since any spin $S > \frac{1}{2}$ would exhibit an anisotropy in a hexagonal lattice. We decided to use two procedures: fitting the spectra either by a single Lorentzian lineshape or by a powder profile. A comparison between the two sets of parameters allows one to determine which aspects of the results are qualitatively robust.
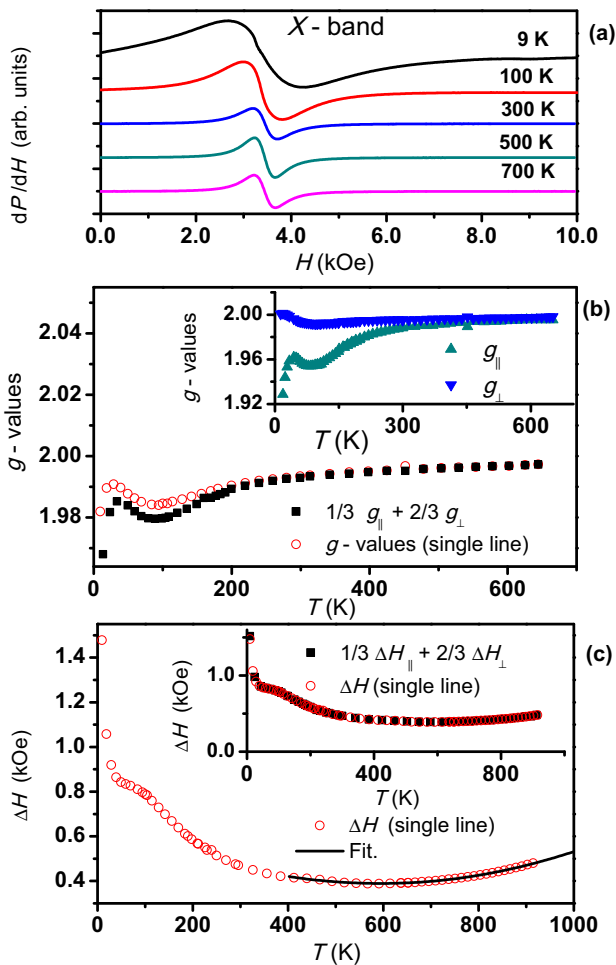

FIG. 7. (Color online) X-band (9.4 GHz) electron spin resonance (ESR) of BaTi$_{1/2}$Mn$_{1/2}$O$_3$. (a) Some representative ESR spectrum lines. (b) Comparison between the ESR g-values, as a function of T, obtained from the single Lorentzian lineshape analysis (single line) and from the powder profile fitting. In the inset, the parameters from the powder profile fitting are shown. (c) ΔH, as a function of T, obtained from the single line analysis. In the high-T region, the thick black line corresponds to analysing ΔH by considering the usual Kubo–Tomita formula plus an activated behavior [Eq. (7)]. In the inset, we compare the single line analysis with the powder profile fitting.

By fitting the spectra with a powder profile, we are under the assumption that the system anisotropy can be described by a g tensor with two components, one of which is an in-plane g-value ($H||ab$, $g_{||}$) and the other is an out-of-plane g-value ($H||c$, $g_\perp$). Experiments on single crystals would allow a proper investigation of the anisotropy of the ESR parameters which would be of great importance to confirm the existence of dimers and trimers in the system [26].

In reference to the results presented in Fig. 5(b), one expects distinct regimes for the behavior of the ESR parameters. At the high-T region (to be understood as the region at which $T > J_a/k_B \approx 200$ K) the ESR will reflect the local moment characteristics. With lowering temperature, the dimerizing spins will stop contributing to the ESR and the response of the magnetic trimers, along with the response of the orphan spins, will dominate. Hence, one expects a crossover behavior in the region of intermediate temperatures with energy scales given by the exchange constants J_a and J_b [26–28].

In Fig. 7(b), we present the ESR g values. In general, the g-values obtained by means of a single-Lorentzian line fitting (full squares) are weakly temperature dependent at high-T, assuming a value close to $g = 1.99$, expected for transition metal ions with small spin-orbit coupling [29]. Around $T = 200$ K, and with lowering temperature, one observes a more conspicuous drop in the g-values. These values are compared with $g' = 1/3 g_{||} + 2/3 g_\perp$ (open circles), where $g_{||}$ and $g_\perp$ are the parameters obtained from the powder fitting. It is shown that $g \approx 1/3 g_{||} + 2/3 g_\perp$ over the entire temperature range. In the inset, $g_{||}$ and $g_\perp$ are presented separately. At high-T, both parameters converge for $g_{||} \approx g_\perp = 1.99$. In the low-$T$ region, $g_\perp$ is nearly constant, whereas there is a clear drop of $g_{||}$. Therefore, the low-T behavior of the g-values is mainly due to the T-dependency of $g_{||}$. Put together, these results suggest that the system develops an easy axis anisotropy as the temperature decreases, starting at about $T \approx 200$ K.

This easy-axis anisotropy is most likely related to the formation of the trimers, since the energy scale of the correlation between the orphan spins, $\theta = 7.7\,(2)$ K, is significantly lower. In this direction, one can see a clear upturn in the g-values at about $T \approx 100$ K, which coincides with the temperature at which the trimer susceptibility [Fig. 5(b)] becomes dominant over the dimer response. Thus, the evolution of the g-values can be connected to the energy scales given by the exchange constants J_a and J_b.

The evolution of ΔH with T is presented in Fig. 7(c). In concentrated systems of transition-metal oxides, a strong exchange narrowing effect will usually make the spectra from powdered samples resemble a single-Lorentzian lineshape, with some distortion due to the underlying anisotropy [30,31]. In practice, it is usual in these situations to analyze the spin dynamics, as expressed by ΔH, in terms of a single-Lorentzian fitting, or in terms of the more crude peak-to-peak distance [32–34]. Here, we first follow the former phenomenological approach and then we briefly compare these results with those from a more accurate analysis based on the powder profile fitting.

In the low-T region, one expects that the linewidth due to the dimers should go to zero, whereas the response due to orphans

and trimers should diverge. The shoulder in ΔH around $T = 100$ K may be associated with this crossover at which the trimer response becomes dominant over the dimer. At high-T, the system should follow the Kubo–Tomita formula, converging for a constant value of $\Delta H_\infty^{\mathrm{high}\,T}$ for $T \gg J_a/k_B = 200$ K. However, a timid increase of ΔH is observed. We fit this behavior with a phenomenological model that reads

$$\Delta H\,(T) = \frac{(1/T)}{[1/(T+\theta)]}\Delta H_\infty^{\mathrm{high}\,T} + A\exp(-\Delta/k_B T)\,. \quad (7)$$

The first term in Eq. (7) is due to the Kubo–Tomita formula and expresses the relaxation mechanism due to the exchange coupling between the spin states in the system. We obtained $\Delta H_\infty^{\mathrm{high}\,T} = 282(4)$ Oe, indicating that anisotropic spin interactions are relatively small at high-T, as it is also indicated by the g-values. The parameters of the second term are $A = 8.9(7) \times 10^3$ Oe and $\Delta/k_B = 3832\,(92)$ K. As is well known [29], one expects an Orbach mechanism to produce an exponential increase of the linewidth. However, it is certain that $\Delta/k_B = 3832\,(92)$ K is much too high an energy scale to be associated with phonons. This situation was associated with different Jahn–Teller distortions, which are close in energy [26]. Hence, $\Delta/k_B = 3832\,(92)$ K would correspond to the energy barrier separating two Jahn–Teller distortions.

The inset of the figure displays a comparison between ΔH, as obtained from the single-line fitting, and the parameters $\Delta H_\parallel$ and $\Delta H_\perp$, from the powder profile fitting. It is again suggested that the system has an easy-axis anisotropy [since $\Delta H \approx (1/3)\Delta H_\parallel + (2/3)\Delta H_\perp$].

We should also comment on some Q-band measurements (not shown). In the presence of an inhomogeneous distribution of Mn sites, one could expect an inhomogeneous broadening of the resonance. This would appear as a field-dependent broadening of the ESR linewidth. Therefore, the sample was also measured at Q band to check for these inhomogeneities and the resonance was found to be homogeneous.

IV. SUMMARY

The structural and magnetic properties of $BaMn_{1/2}Ti_{1/2}O_3$ were investigated. A scenario was formulated under which the magnetism of the system stems from the formation of magnetic dimers and trimers of Mn cations, coexisting with a population of orphan spins. This scenario resulted in a good description of the susceptibility of the system in the whole temperature interval. The dimers are formed by means of a strong first-neighbor exchange constant J_a, whereas the trimers require a second neighbor exchange constant J_b which competes with J_a. This competition introduces frustration in the magnetic response of the Mn trimers and was captured by our ESR experiment, as discussed in the context of the temperature dependence of the g-values. Thus, it is proposed that $BaTi_{1/2}Mn_{1/2}O_3$ is a rare case of an intrinsically disordered $S = \frac{3}{2}$ spin-gap system, with energy scales given by $J_a/k_B = 200\,(2)$ K and $J_b/k_B = 130\,(10)$ K. The deduced ground state is magnetic and frustrated, connecting the physics of spin-gap and frustrated systems. Inelastic neutron scattering experiments would be highly instrumental to test the spin gap, whereas susceptibility and specific heat at further lower temperatures are required to investigate the frustrated ground state.

[1] E. Dagotto, Science **309**, 257 (2005).

[2] T. Aharen, J. E. Greedan, F. Ning, T. Imai, V. Michaelis, S. Kroeker, H. Zhou, C. R. Wiebe, and L. M. D. Cranswick, Phys. Rev. B **80**, 134423 (2009).

[3] R. Moessner and A. P. Ramirez, Phys. Today **59**(2), 24 (2006).

[4] L. Balents, Nature (London) **464**, 199 (2010).

[5] T. Aharen, J. E. Greedan, C. A. Bridges, A. A. Aczel, J. Rodriguez, G. MacDougall, G. M. Luke, T. Imai, V. K. Michaelis, S. Kroeker *et al.*, Phys. Rev. B **81**, 224409 (2010).

[6] M. A. de Vries, A. C. Mclaughlin, and J.-W. G. Bos, Phys. Rev. Lett. **104**, 177202 (2010).

[7] E. Granado, J. W. Lynn, R. F. Jardim, and M. S. Torikachvili, Phys. Rev. Lett. **110**, 017202 (2013).

[8] G. M. Keith, C. A. Kirk, K. Sarma, N. M. Alford, E. J. Cussen, M. J. Rosseinsky, and D. C. Sinclair, Chem. Mater. **16**, 2007 (2004).

[9] T. Nikuni, M. Oshikawa, A. Oosawa, and H. Tanaka, Phys. Rev. Lett. **84**, 5868 (2000).

[10] T. Nakajima, H. Mitamura, and Y. Ueda, J. Phys. Soc. Jpn. **75**, 054706 (2006).

[11] H. Tsujii, B. Andraka, M. Uchida, H. Tanaka, and Y. Takano, Phys. Rev. B **72**, 214434 (2005).

[12] M. Hase, M. Soda, T. Masuda, D. Kawana, T. Yokoo, S. Itoh, A. Matsuo, K. Kindo, and M. Kohno, arXiv:1404.6297.

[13] E. C. Andrade and M. Vojta, Europhys. Lett. **97**, 37007 (2012).

[14] A. Lavarélo, G. Roux, and N. Laflorencie, Phys. Rev. B **88**, 134420 (2013).

[15] B. Ravel and M. Newville, J. Synchrotron Radiat. **12**, 537 (2005).

[16] A. C. Larson and R. B. Von Dreele, General Structure Analysis System (GSAS), Los Alamos National Laboratory Report No. LAUR 86-748, 2004.

[17] B. H. Toby, J. Appl. Crystallogr. **34**, 210 (2001).

[18] G. Subías, J. García, M. G. Proietti, and J. Blasco, Phys. Rev. B **56**, 8183 (1997).

[19] M. Croft, D. Sills, M. Greenblatt, C. Lee, S.-W. Cheong, K. V. Ramanujachary, and D. Tran, Phys. Rev. B **55**, 8726 (1997).

[20] M. Sikora, Cz. Kapusta, K. Knížek, Z. Jirák, C. Autret, M. Borowiec, C. J. Oates, V. Procházka, D. Rybicki, and D. Zajac, Phys. Rev. B **73**, 094426 (2006).

[21] L. Miranda, A. Feteira, D. C. Sinclair, K. Boulahya, M. Hernando, J. Ramírez, A. Varela, J. M. González-Calbet, and M. Parras, Chem. Mater. **21**, 1731 (2009).

[22] R. D. Shannon, Acta Crystallogr., Sect. A: Cryst. Phys., Diffr., Theor. Gen. Crystallogr. **32**, 751 (1976).

[23] P. Schiffer and I. Daruka, Phys. Rev. B **56**, 13712 (1997).

[24] N. W. Ashcroft and N. D. Mermin, *Solid State Physics* (Holt, Rinehart and Winston, New York, 1976).

[25] R. M. White, *Quantum Theory of Magnetism Magnetic Properties of Materials* (Springer, Berlin, 2007).

[26] J. Deisenhofer, R. M. Eremina, A. Pimenov, T. Gavrilova, H. Berger, M. Johnsson, P. Lemmens, H.-A. Krug von Nidda, A. Loidl, K.-S. Lee *et al.*, Phys. Rev. B **74**, 174421 (2006).

[27] J. Deisenhofer, S. Schaile, J. Teyssier, Z. Wang, M. Hemmida, H.-A. K. von Nidda, R. M. Eremina, M. V. Eremin, R. Viennois, E. Giannini *et al.*, Phys. Rev. B **86**, 214417 (2012).

[28] D. V. Zakharov, J. Deisenhofer, H.-A. Krug von Nidda, P. Lunkenheimer, J. Hemberger, M. Hoinkis, M. Klemm, M. Sing, R. Claessen, M. V. Eremin *et al.*, Phys. Rev. B **73**, 094452 (2006).

[29] A. Abragam and B. Bleaney, *Electron Paramagnetic Resonance of Transition Ions* (Clarendon Press, Oxford, 1970).

[30] P. W. Anderson and P. R. Weiss, Rev. Mod. Phys. **25**, 269 (1953).

[31] D. L. Huber, Phys. Rev. B **12**, 31 (1975).

[32] M. T. Causa, M. Tovar, A. Caneiro, F. Prado, G. Ibanez, C. A. Ramos, A. Butera, B. Alascio, X. Obradors, S. Pinol *et al.*, Phys. Rev. B **58**, 3233 (1998).

[33] D. L. Huber, G. Alejandro, A. Caneiro, M. T. Causa, F. Prado, M. Tovar, and S. B. Oseroff, Phys. Rev. B **60**, 12155 (1999).

[34] D. Zakharov, J. Deisenhofer, H.-A. von Nidda, A. Loidl, T. Nakajima, and Y. Ueda, Phys. Rev. B **78** (2008).